

Predictions of Microstructures when Welding Automotive Advanced High-Strength Steels

A combination of thermal and microstructural modeling can be used to estimate performance of welds in advanced high-strength steels

BY J. E. GOULD, S. P. KHURANA, AND T. LI

ABSTRACT. Weld strength, formability, and impact resistance for joints on automotive steels are dependent on the underlying microstructure. A martensitic weld area is often a precursor to reduced mechanical performance. In this paper, efforts are made to predict underlying joint microstructures for a range of processing approaches, steel types, and gauges. This was done first by calculating cooling rates for some typical automotive processes [resistance spot welding (RSW), resistance mash seam welding (RMSEW), laser beam welding (LBW), and gas metal arc welding (GMAW)]. Then, critical cooling rates for martensite formation were calculated for a range of automotive steels using available thermodynamically based phase transformation models. These were then used to define combinations of process type, steel type, and gauge where welds could be formed avoiding martensite in the weld area microstructure.

Introduction

Manufacturability, fuel economy, performance, and styling all continue to be major considerations in the design of next-generation vehicles. A major consideration in these improvements is material selection. To achieve these results in the body-in-white structure, automakers are increasingly turning to alternate materials. Materials under consideration include plastics, aluminum, and advanced high-strength steels (AHSS) (Ref. 1). In recent years, considerable interest has been placed on the use of Al sheet (Refs. 2, 3). However, material cost considerations have created renewed interest in the use of steels for advanced body construction (Ref. 4). Steels available today range from the highly formable interstitial-free (IF) grades to the range of AHSS materials. Interstitial-free grades of steel contain very

low carbon contents, typically less than 0.010%. These materials offer both high R values (indicating resistance to sheet thinning during forming) and tensile ductilities in excess of 50%. Such materials have enabled complex forming operations, as well as reductions in forming-related scrap. Advanced high-strength steels are now available with tensile strengths ranging from 300 to 1500 MPa (Refs. 5, 6). Such steels employ a range of hardening mechanisms. The lower end of these strength ranges is typically solid-solution strengthened, particularly with phosphorus additions. Intermediate grades are generally made up of dual-phase (DP) steels, employing a fine grain structure and mixture of ferrite and martensite phases. More recent variants on such steels include the transformation-induced plasticity (TRIP) and complex-phase (CP) steels. The former uses a mixture of ferrite and austenite in the microstructure, while the CP grades employ mixtures of ferrite, bainite, and martensite. These steels largely offer improvements in vehicle weight through gauge reduction. Currently, body skin panels are on the order of 0.8 mm. Gauge reductions down to 0.6 mm are being considered for AHSS skins. In addition to direct replacement of skin panels, selectively placed AHSS offer potential for improved impact and fatigue performance, offering additional potential for vehicle weight reductions.

Efforts to implement these steels have, however, been accompanied by welding-

related problems. Since the body-in-white is largely assembled by RSW, most problems have been associated with that joining approach. Recent work has related many of these welding problems to the formation of martensites in the weld nugget (Refs. 7, 8). Martensite, particularly with increasing carbon contents, results in weld zones with hardness levels sufficient to fail in a brittle manner on loading. Similar observations have been made when LBW these higher-strength grades of steel (Refs. 9, 10). The hardness achieved in these steels is directly associated with the cooling rates implicit in these processes. Cooling rates for many automotive welding methods are difficult to measure, largely related to the high processing speeds implied by these technologies (Ref. 11). These cooling rates have, however, been estimated by a range of modeling techniques. These include both closed form (Refs. 12–14) and numerical approaches (Refs. 15–17). These analyses have shown that such automotive processes can achieve cooling rates on the order of 10^5 °C/s. Assessment of microstructural changes at these cooling rates is difficult, particularly because accomplishing such cooling rates outside the processes themselves is difficult to nearly impossible. Recently, however, efforts to model austenite decomposition have offered new tools in predicting weld microstructures at these cooling rates. These approaches are both thermodynamically (Ref. 18) and phenomenologically (Ref. 19) based, and are capable of predicting continuous cooling transformation (CCT) diagrams for both a wide range of steels and cooling rates.

In this research, efforts have been made to predict cooling rates for a range of steel gauges welded with a number of automotive welding processes. These processes include RSW, RMSEW, LBW, and GMAW. Cooling rates are calculated using a range of closed-form solutions available in the literature for a range of

KEYWORDS

High-Strength Steels
Resistance Spot Welding
Resistance Mash Seam Welding
Laser Beam Welding
Gas Metal Arc Welding
Thermal Modeling
Microstructural Modeling

J. E. GOULD, S. P. KHURANA, and T. LI are with Edison Welding Institute, Columbus, Ohio.

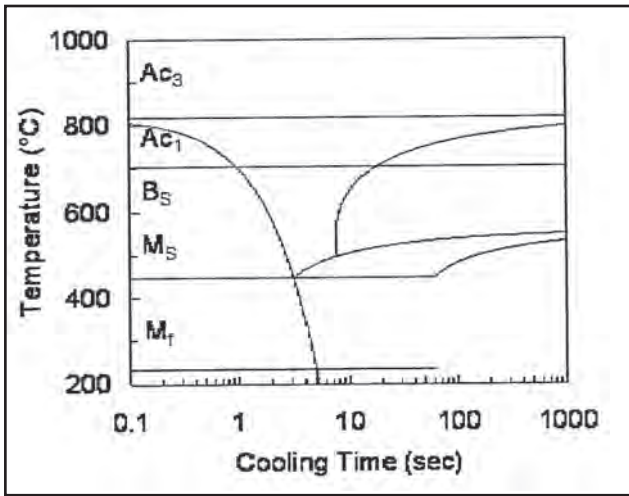


Fig. 1 — CCT diagram for a representative DP 600 steel based on the model developed by Li (Ref. 18).

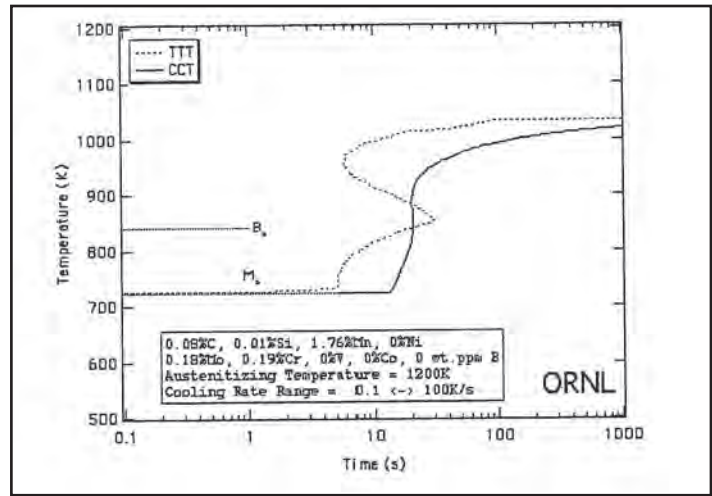


Fig. 2 — CCT/TTT diagram for a representative DP 600 steel based on the model developed by Bhadeshia (Ref. 19).

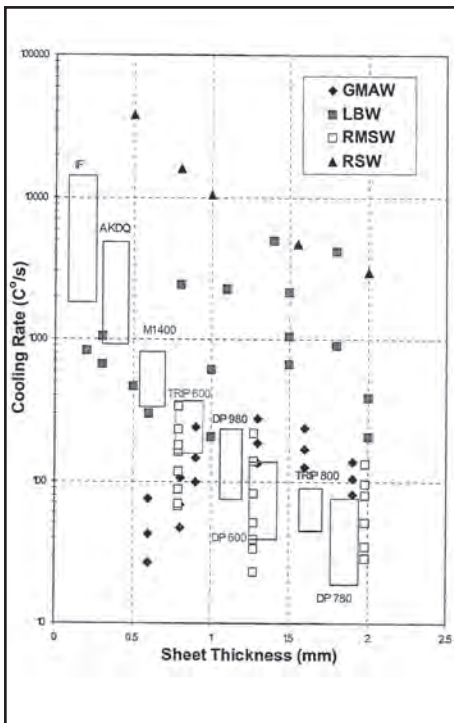


Fig. 3 — Cooling rates as a function of gauge for the RSW, RMSEW, LBW, and GMAW processes. [Also included are critical cooling rates for a number of automotive-type sheet steels. The top of the range is taken from the model of Li (Ref. 18) and the bottom of the range is taken from Bhadeshia (Ref. 19).]

gauges of automotive interest. These results are then compared to critical cooling rates (for a martensite formation) for a number of new-generation automotive sheet steels. The comparison is then used to predict combinations of materials, gauges, and processes that might be problematic in automotive manufacture. Some microstructural evidence is also presented supporting the modeling results.

Table 1 — Definition of Terms for Predicting the Fractions of Constituent Phases in the Final Microstructure

	Ferrite Formation	Pearlite Formation	Bainite Formation
ΔT	$Ae_3 - T$	$Ae_1 - T$	$Bs - T$
n	3	3	2
Q	27,500	27,500	27,500
F (Composition, G)	$F_{\text{ferrite}}/20.41G$	$F_{\text{pearlite}}/20.32G$	$F_{\text{bainite}}/20.29G$
F	$[\exp(1.00 + 6.31C + 1.78Mn + 0.31Si + 1.12Ni + 2.70Cr + 4.06Mo)]$	$[\exp(-4.25 + 4.12C + 4.36Mn + 0.44Si + 1.71Ni + 3.33Cr + 5.19\sqrt{Mo})]$	$[\exp(-10.23 + 10.18C + 0.85Mn + 0.55Ni + 0.90Cr + 0.36Mo)]$

Analytical Models for Predicting Cooling Rates

Cooling rates during RSW have been calculated (Ref. 14) based on the following assumptions:

1. Heat flow during RSW is essentially one dimensional, from the workpiece into the electrodes.
2. The peak temperature distribution in the resistance spot weld can be described by a sine wave half period, with the peak at the center between the electrodes.
3. The welding electrodes are essentially straight sided.

Based on these observations, cooling rates during RSW can be estimated by the following equation:

$$\frac{\partial \Theta}{\partial t} = - \left(\frac{\alpha \pi^2}{4 \Delta x^2} \right) \left(\frac{\Theta}{\Theta_p} \right) \left(\Theta_p - \frac{\Theta}{1 + \left(\frac{2}{\pi} \right) \left(\frac{k_E}{k_S} \right) \left(\frac{\Delta x}{\Delta x_E} \right) \cos \left(\frac{\pi}{2 \Delta x} x \right)} \right) \quad (1)$$

where Θ is the temperature, t is time, α is the thermal diffusivity, Δx and Δx_E are the sheet and electrode face thicknesses, respectively, Θ_p is the peak temperature in the spot weld, k_E and k_S are the thermal conductivities of the electrode material (Cu) and steel, respectively, and x is the position through the spot weld.

Similar equations can be obtained for the continuous processes (RMSEW, LBW, GMAW) based on the Rosenthal equations (Ref. 12). For automotive applications, the 2D approaches are the most appropriate. The basic equation, as modified by Adams (Ref. 13) to predict peak cooling rates, is as follows:

$$\frac{\partial \Theta}{\partial t} = - \frac{2 \pi k_s^2}{\alpha} \left(\frac{v \Delta x}{Q} \right)^2 (\Theta - \Theta_o)^3 \quad (2)$$

where v is the travel speed, Q is the power input, and Θ_o original base metal temperature. Q for the LBW and GMAW processes can be calculated directly, and inserted into the equation. This equation has also been modified to estimate cooling rates during RMSEW (Ref. 20). In this case, the power input is estimated from the applied current and geometry of the lap. The resulting

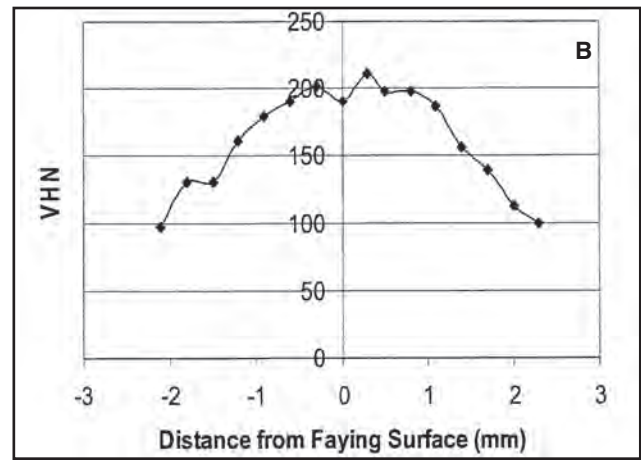
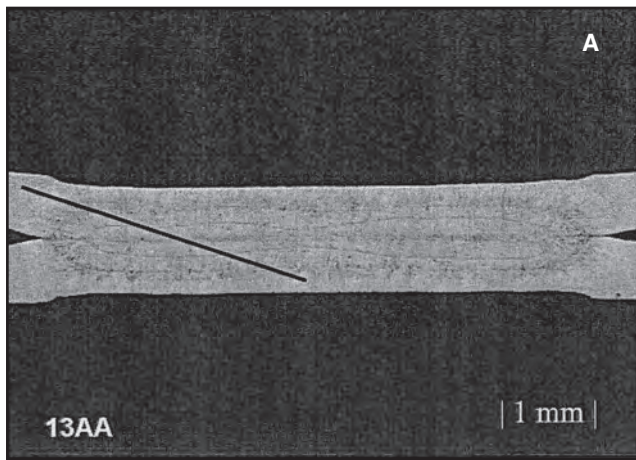


Fig. 4 — Macrostructure and hardness profile of a resistance spot weld on 0.8-mm IF (0.007% C, 0.14% Mn) steel. A — Macrostructure, hardness profile trace is shown as a dark line; B — hardness profile.

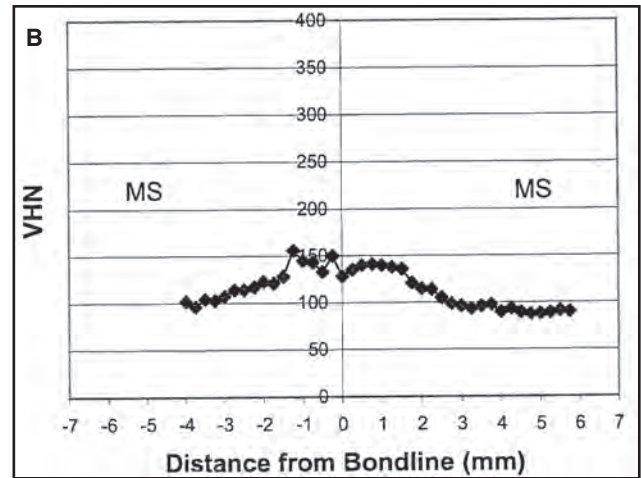
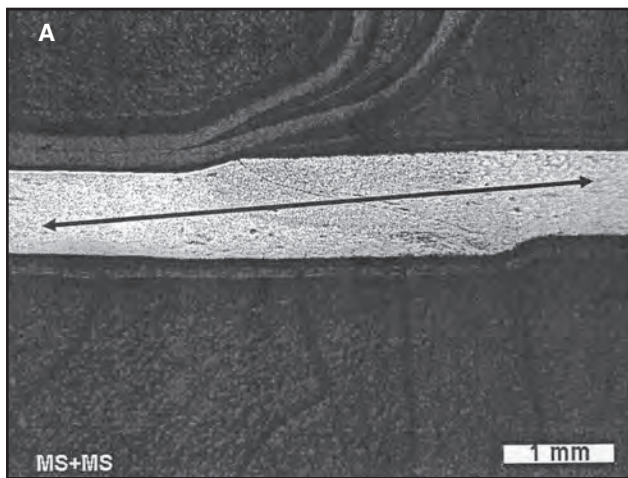


Fig. 5 — Macrostructure and hardness profile of a resistance mash seam weld on 0.8-mm AKDQ (0.03% C, 0.3% Mn) steel. A — Macrostructure, hardness profile trace is shown as a dark line; B — hardness profile.

equation is

$$\frac{\partial \Theta}{\partial t} = -\frac{2\pi k_s^2}{\alpha} \left[\frac{v}{\rho \left(\frac{I}{A} \right)^2 l y_o} \right]^2 (\Theta - \Theta_o)^3 \quad (3)$$

where ρ is the resistivity of steel, I is the welding current, A is the effective wheel contact area, l is the length of wheel contact, and y_o is the original overlap of the two sheets. These equations are now to be used to estimate cooling rates as a function of gauge for the range of welding technologies used in automotive manufacture today.

Prediction of Critical Cooling Rates for Martensite Formation

The critical cooling rates can be determined from CCT diagrams. As mentioned

previously, mathematical models have been developed to define these CCT diagrams. These models generally consist of a thermodynamics portion, which determines the equilibrium temperatures, and an austenite decomposition reaction kinetics portion, which predicts the resultant microstructure. Two such models have been developed by Li (Ref. 18) and Bhadeshia (Ref. 19).

In the model developed by Li (Ref. 18), thermodynamic calculations are used to determine Ae_3 and Ae_1 temperatures. In addition, the thermodynamic conditions for the three-phase, $\alpha + \gamma +$ cementite, equilibria are also computed. The equations defining the transformation temperatures Ae_3 and Ae_1 are given in Table 1.

A reaction kinetics model can then be used to predict CCT diagrams. The reaction kinetics model (Ref. 18) is described by the following equations.

$$\tau(X, T) = \frac{F(\text{Composition}, G)}{\Delta T^n \exp(-Q/RT)} S(X) \quad (4)$$

where $\tau(X, T)$ is the isothermal time taken to reach X amount of transformation at T temperature, ΔT is the undercooling, n is an empirical constant, Q is the activation energy, F is a function of steel composition, G is the prior austenite grain size in ASTM, and $S(X)$ is explained by the following equation.

$$S(X) = \int_0^X \frac{1}{X^{0.4(1-X)} (1-X)^{0.4X}} dX \quad (5)$$

Combining these equations and differentiating, we get the following:

$$\frac{dX}{dt} = \frac{\Delta T^n \exp(-Q/RT) X^{0.4(1-X)} (1-X)^{0.4X}}{F(\text{Composition}, G)} \quad (6)$$

The individual terms of this equation are defined in Table 1.

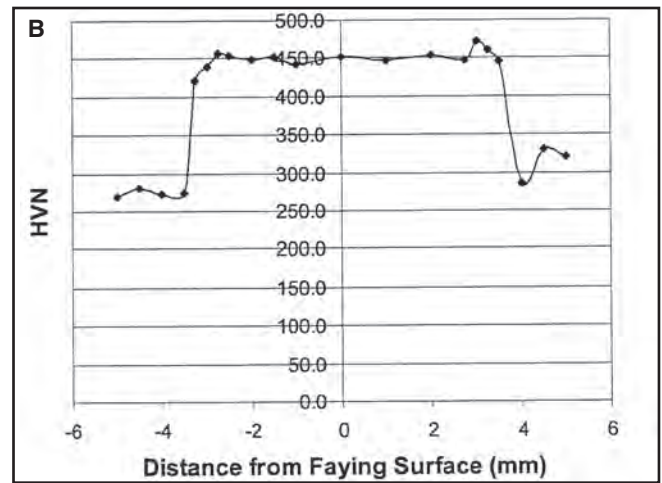
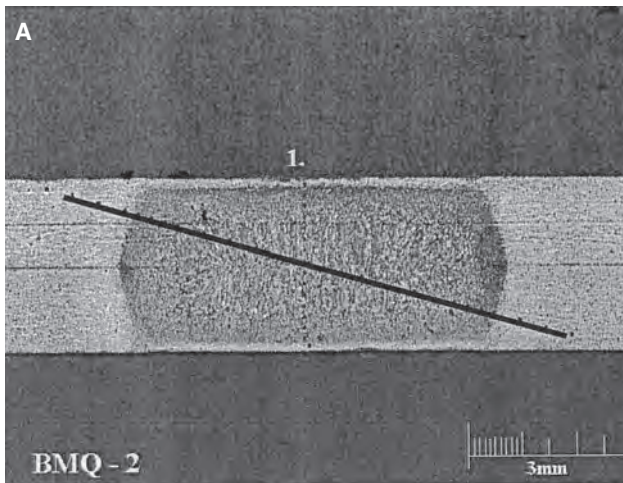


Fig. 6 — Macrostructure and hardness profile of a resistance spot weld on 1.6-mm DP980 (0.15% C, 1.4% Mn) steel. A — Macrostructure, hardness profile trace is shown as a dark line; B — hardness profile.

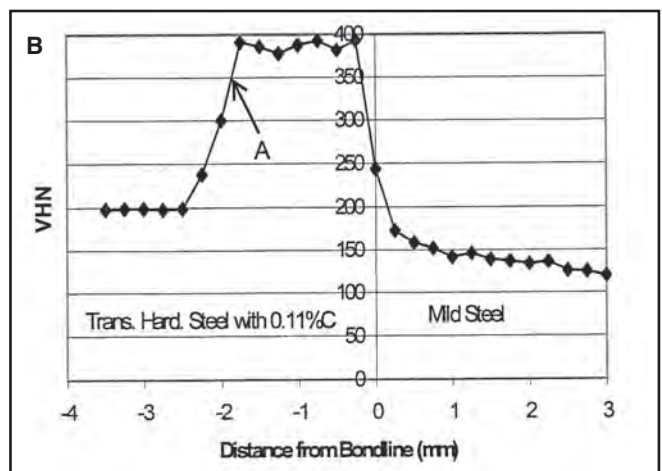
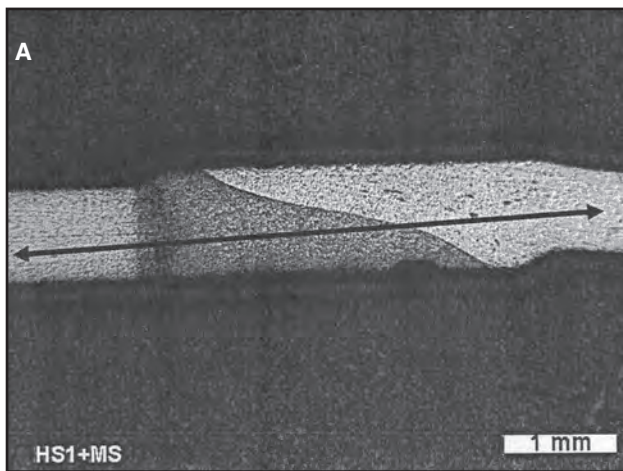


Fig. 7 — Macrostructure and hardness profile of a resistance mash seam weld between 0.8-mm DP980 and AKDQ steel.

The preceding equations can then be used to calculate the fractions of constituent phases as a function of time and temperature. This provides the basis for the appropriate CCT diagram. An example of a resulting predicted CCT/TTT diagram for a DP 600 steel is given in Fig. 1.

In the approach by Bhadeshia (Ref. 19), a thermodynamic method has been used to allow the prediction of phase transformation from the chemical composition of the steel concerned. In this case, the TTT diagram has been treated as composed of two overlapping C-curves. One C-curve represents the diffusional polygonal ferrite, the displacive Widmanstätten ferrite and pearlite transformations, and the other C-curve represents the bainite reactions. The correct prediction of the C-curves is based on estimating the shift in these curves as a function of alloying elements.

The time period before the detectable amount of a phase is formed at an isother-

mal temperature is used to detect this shift. This time period is dependent on the nucleation of the phase. The incubation period of a phase, τ , is defined in terms of time taken to establish a steady-state nucleation rate.

$$\tau \propto \frac{T}{(\Delta F_m^v)^p D} \quad (7)$$

where T is the absolute temperature, ΔF_m^v is the maximum volume free energy change accompanying the formulation of a nucleus in a large amount of matrix phase, P is a constant, and D is an effective diffusion coefficient defined as

$$D \propto \exp\left(\frac{S}{R}\right) \exp\left(-\frac{Q}{RT}\right) \quad (8)$$

where S is the activation entropy for diffusion, Q is the activation enthalpy for diffusion, and R is the gas constant.

Substituting Equation 8 in Equation 7,

$$\ln\left[\frac{(\Delta F_m^v)^p \tau}{T}\right] = \frac{Q}{RT} + C_1 \quad (9)$$

where ΔF_m is ΔF_m for 1 mol and C_1 is a constant.

Optimum values of p and Q are obtained by substituting experimental values of T , ΔF_m^v , and τ , and varying p until the equation balances.

Bhadeshia (Ref. 19) noticed that the graph of $\ln[(\Delta F_m^v)^p \tau / T]$ against $1/RT$ exhibited systemic curvature and did not have the strict linear form applied by Equation 9. This is attributed to the fact that activation enthalpy and entropy are

temperature dependent. So Equation 9 was modified to the following form.

$$\ln \left[\frac{\Delta F_m^p \tau}{T^z} \right] = \frac{Q'}{RT} + C_4 \quad (10)$$

where z , Q' , and C_4 are constants.

This equation predicted better results. The correlation coefficients of Equation 10 were also better than that of Equation 9. The resulting CCT diagrams were used by Babu (Ref. 21) for predictions of microstructures in resistance spot welds, and can also be accessed online at the ORNL Web site (Ref. 22). A representative CCT/TTT curve based on this approach is presented in Fig. 2.

Comparisons of Process Cooling Rates and Critical Cooling Rates for Martensite Formation

The equations described above have been used here to calculate cooling rates over a range of automotive-related steel gauges. Welding parameters (e.g., power inputs, welding speeds) have been taken from available reference texts (Refs. 23–26). The resulting cooling rates, as a function of gauge, are shown collectively in Fig. 3. Of the processes, RSW shows the highest cooling rates. These rates range from over 100,000°C/s for gauges less than 0.5 mm, to roughly 2000°C/s at a 2.0-mm gauge. Of note, RSW is the only process examined here showing such a gauge effect. Cooling rates for LBW are somewhat less, ranging from 200° to 5000°C/s, depending on the specific parameters used. The scatter in the cooling rates here is an artifact of the recommended practices from the reference text (Ref. 25). Cooling rates for GMAW and RMSEW are similar, ranging from 20° to 300°C/s, again depending on the specific parameters used.

Critical cooling rates to achieve martensite formation for a range of automotive steels were taken from CCT diagrams determined using the two computational approaches described previously. Input to these models included the specific chemistry and grain size of each steel. Chemistries for the representative steels are given in Table 2. The resulting CCT curves were used to estimate the specific cooling rate(s) distinguishing 100% martensite formation. The characteristic cooling rates for each of these steels (using the respective models) are also provided in Table 2. It is first of note that depending on steel composition and the phase transformation model used, critical cooling rates range from 10¹ to 10⁴ °C/s. In particular, it is noted that the model by Li (Ref. 18) predicts critical cooling rates 2 to 7 times that

Table 2 — Compositions and Critical Cooling Rates (for Martensite Formation) for the Steels of Interest in this Study

Composition/ CoolingRate (%)	Steel of Interest							
	IF	AKDQ	DP 600	DP 780	DP 980	M 1400	TRIP 600	TRIP 800
C	0.007	0.06	0.08	0.1	0.15	0.19	0.09	0.21
Mn	0.15	0.3	1.76	2.33	1.38	0.47	1.45	1.7
Si	—	—	0.01	0.23	0.29	0.02	1.47	1.66
Cr	—	—	0.19	0.03	0.03	—	0.05	0.03
Mo	—	—	0.18	0.02	0	—	0.1	0
Al	0.03	0.03	0.05	0.04	0.04	0.03	0.03	0.04
V	—	—	0	0.06	0	—	0.01	0
Ti	0.05	—	0	0	0.01	—	0.01	0.01
Crit. Cooling Rate (°C/s) based on Li ⁽¹⁸⁾	13,500	5000	120	70	225	800	315	90
Crit. Cooling Rate (°C/s) based on Bhadeshia ⁽¹⁹⁾	2000	1000	40	18	75	320	140	45

for similar steels by Bhadeshia (Ref. 19). In addition, the gap tends to widen for the leanest alloyed steels [IF and aluminum-killed drawing quality (AKDQ)]. The models do, however, bracket the regimes of critical cooling rates for each of the respective grades of steels.

These ranges of critical cooling rates for martensite formation are superimposed onto Fig. 3. These are shown as a series of boxes labeled for each respective steel. The top of the box represents the cooling rate predicted by the Li model (Ref. 18) and the bottom that for the Bhadeshia model (Ref. 19). In Fig. 3, the cooling rates above that indicated by these respective levels (for the steel of interest) result in martensitic welds, while those below will result in a mixture of austenitic decomposition products. Effectively, processes with implied cooling rates above that indicated for the respective steel would contain predominantly martensite in the weld zone, and be susceptible to undesirable modes of failure. Those processes showing less than the critical cooling rate (for the respective steel) will result in tougher microstructures and improved performance.

From Fig. 3, it is clear that the critical cooling rates decrease with the increasing complexity of the steel (higher alloying content) and strength level. This is largely an artifact of the strengthening mechanisms employed in the higher-strength products. Higher-strength grades of steels generally employ larger volume fractions of second phases (bainite, martensite, austenite), typically accomplished by increases in austenite stabilizing additions. The most common of these are carbon and Mn, although high compositions of Si are present in the TRIP steels. These chemistry variations appear capable of sup-

pressing the critical cooling rates to values near 10°–100°C/s, compared to the 1000°–5000°C/s values reported here for the common mild steel grades used in automotive production.

Figure 3 suggests the IF, AKDQ (mild steel), and even the martensite 1400 grades will decompose without martensitic transformation when joined with either the GMAW or RMSEW welding processes. The IF and AKDQ grades, alternately may or may not form martensite when joined with RSW or LBW, depending on the processing conditions used. For these steels, however, carbon contents are sufficiently low that martensite in the joint is not a precursor to unacceptable modes of failure.

Some examples of welds made on 0.8-mm IF and AKDQ grades of steels (Ref. 9) are presented in Figs. 4 and 5. Figure 4 shows a cross section of a resistance spot weld made on an IF grade of steel, as well as the associated hardness profile. The hardness profile is seen to progressively increase from the base metal to the center of the weld. Equation 1 suggests that cooling rates also will increase progressively from the electrode contact surface to the workpiece faying surface. This, in effect, shows that for this weld, cooling rate and hardness are related. This relationship suggests a lack of athermal martensite. With athermal martensite, hardness would be independent of cooling rate from an austenitic microstructure. Rather, the hardness variations observed are related to the scale of the microstructure and evolving constituent phases. This suggests that the IF steel welded here has a critical cooling rate for martensite formation greater than that provided by resistance welding. These results are more consistent with the model of Li than Bhadeshia. A microstructure and

hardness profile of a RMSEW made between two pieces of AKDQ steel is shown in Fig. 5. The hardness profile for this weld peaks at the centerline, and is characteristic of the slower cooling rates inherent in this process.

Figure 3 suggests that the AHSS will all easily transform to martensite during RSW and for most LBW. In these cases, carbon levels are now sufficient such that the formed martensite can experience brittle fracture (Refs. 7, 8). For other welding processes (GMAW and RMSEW), the welds may or may not transform to martensite, depending on the processing conditions used and the specific chemistry of the steel. The most heavily alloyed steels (TRIP 800 and DP 780) do appear likely to form martensite in any of the automotive welding processes.

Some examples of welds made with a DP 980 grade of steel (Ref. 27) are presented in Figs. 6 and 7. Figure 6 shows a cross section and hardness profile for a resistance spot weld made on the 1.6-mm DP 980. The hardness profile of the weld shows a typical "top hat" morphology. This shows that for resistance spot welds made on this metal, hardness (for regions exceeding the austenization temperature) is largely independent of cooling rate, and consistent with athermal martensite formation. A similar cross section and hardness trace for a resistance mash seam weld made between 0.8-mm DP 980 and AKDQ steels are presented in Fig. 7. In this case, the DP 980 side of the joint shows the top hat hardness profile suggesting martensite formation. This again can be nominally predicted from either microstructural model, depending on the weld processing employed. The AKDQ steel side of the weld shows hardness variations nearly identical to that described in Fig. 5.

One particular feature of note is variability in critical cooling rates for the different grades of AHSS, particularly that the DP 980 steel evaluated shows critical cooling rates higher than either the DP 600 or 780 grades. This variation in critical cooling rate largely is related to the relative carbon and Mn contents of the respective steels. Both are hardenability additions, and critical to the processing required in order to achieve desired mechanical properties. However, lower carbon contents (reducing both hardenability and martensite hardness) in the DP 600 and 780 steels are offset by substantially higher (nearly a factor of 2) Mn contents. This results in a higher hardenability for these steels, even though the actual design strengths are reduced. It also raises concern that differing formulations from different steel suppliers may result in a broad range of critical cooling rates for steels of a given grade. This suggests the possibility that steels of a given grade can actually vary in and out of conditions for form-

ing martensite with a given process, resulting in intermittent weld failures on a production floor.

Conclusions

In this work, closed-form solutions were used to calculate cooling rates for a range of automotive-related welding processes (RSW, RMSEW, LBW, and GMAW) as a function of gauge. In addition, available microstructural models were used to predict critical cooling rates for a number of automotive-related sheet steel products. The results were used to investigate combinations of processes, steel types, and gauge ranges, which could result in detrimental martensite in the weld area. The results showed that highest cooling rates were associated with RSW, followed by LBW, and finally resistance seam welding (RSEW) and RMSEW. It was found that the IF and mild steels could form martensite during either RSW or LBW, but the martensite is of sufficiently low carbon levels to avoid undesirable modes of failure on destructive testing. The AHSS generally showed potential for martensite formation with the RSW and LBW processes. Here, carbon levels are sufficient that the formed martensites can be detrimental to such failure modes during destructive testing. The AHSS also showed potential for martensite formation during RMSEW and GMAW. For these steels and processes, sufficient variation exists in both steel chemistry and implied cooling rates for these processes to show intermittent martensite formation and loss of performance. It was also noted that susceptibility of martensite formation was less dependent on the grade of the AHSS and more on the specific chemistry used to achieve the strength levels required for the grade.

References

1. Dinda, S., and Diaz, R. 1995. The partnership for a new generation of vehicles (PNGV) and its impact on body engineering. *Proc. IBEC 95, Advanced Technologies and Processes*, pp. 5–8, IBEC Ltd.
2. Kurihara, Y. 1993. The role of aluminum in automotive weight reduction, Part I. *Journal of Metals* 45(11): 32–33.
3. Tuler, F., Warren, A., Mariano, S., and Wheeler, M. 1994. Overall benefits and value of aluminum for an automobile body structure. *Proc. IBEC 94, Automotive Body Materials*, pp. 8–14, IBEC Ltd.
4. Crooks, M. J., and Miner, R. E. 1996. The ultralight steel auto body program completes phase I. *Journal of Metals* 48(7): 13–15.
5. Davies, R. G., and Magee, C. L. 1979. Physical metallurgy of automotive high strength steels. *Structure and Properties of Dual Phase Steels*, eds. R. A. Kot and J. W. Morris, AIME.
6. Bleck, W. 1996. Cold rolled, high-strength sheet steels for auto applications. *Journal of Metals* 48(7): 26–30.
7. Gould, J. E., Lehman, L. R., and Holmes,

S. 1996. A design of experiments evaluation of factors affecting the resistance spot weldability of high-strength steels. *Proc. Sheet Metal Welding Conference VII, AWS Detroit Section*.

8. Gould, J. E., and Workman, D. 1998. Fracture morphologies of resistance spot welds exhibiting hold time sensitivity behavior. *Proc. Sheet Metal Welding Conference VIII, AWS Detroit Section*.

9. Shao, H. 2000. Blank welding high strength steels, PhD dissertation. Columbus, Ohio, The Ohio State University.

10. Ream, S. L. 2003. Remote laser weld performance in advanced high strength steels. *Proc. ALAW 2003*. University of Michigan.

11. Gould, J. E. 1987. An examination of nugget development during spot welding using both experimental and analytical techniques. *Welding Journal* 67(1): 1-s to 10-s.

12. Rosenthal, D. 1941. Mathematical theory of heat distribution during welding and cutting. *Welding Journal* 20(5): 220-s to 234-s.

13. Adams, C. M. Jr. 1958. Cooling rates and peak temperatures in fusion welding. *Welding Journal* 37(5): 210-s to 215-s.

14. Chuko, W., and Gould, J. E. 2002. Development of appropriate resistance spot welding practice for transformation-hardened steels - phase 2: evaluation of post-weld cooling rate techniques. Report to the American Iron and Steel Institute.

15. Cho, H. S., and Cho, Y. J. 1989. A study of the thermal behavior in resistance spot welds. *Welding Journal* 68(6): 230-s to 244-s.

16. Xie, J. 2002. Weld morphology and thermal modeling in dual-beam laser welding. *Welding Journal* 81(12): 283-s to 290-s.

17. Kumar, S., and Bhaduri, S. C. 1994. Three-dimensional finite element modeling of gas metal-arc welding. *Metallurgical Transactions B* 25B(3): 435–441.

18. Li, M. V., Niebuhr, D. V., Meekisho, L. L., and Atteridge, D. G. 1998. A computational model for the prediction of steel hardenability. *Metallurgical and Materials Transactions B* 29B(6): 661–672.

19. Bhadeshia, H. K. D. H., and Svensson, L.-E. 1993. *Mathematical Modeling of Weld Phenomena*, eds. H. Cerjack and K. E. Easterling. Institute of Metals, London, pp. 109–180.

20. Gould, J. E. 2003. Theoretical analysis of bonding characteristics during resistance mash seam welding sheet steels. *Welding Journal* 82(10): 263-s to 267-s.

21. Babu, S. S., Reimer, B. W., Santella, M. L., and Feng, Z. 1998. Integrated thermal-microstructure model to predict the property gradients in resistance spot steel welds. *Proc. Sheet Metal Welding Conference VIII, AWS Detroit Section*.

22. <http://engm01.ms.ornl.gov>, Oak Ridge National Laboratory.

23. *Resistance Welding Manual*, 4th ed. Resistance Welding Manufacturing Alliance, George H. Buchanan Co. Philadelphia, Pa., pp. 7–16.

24. Funk, E. J., and Begeman, M. L. 1956. Electrical and metallurgical characteristics of mash seam welds. *Welding Journal* 35(6): 265-s to 274-s.

25. *LIA Handbook of Laser Materials Processing*. Ready, J. F., and Farson, D. F. (eds. in chief), pp. 381 and 399.

26. Cary, H. B. 1979. *Modern Welding Technology*. Englewood Cliffs, N.J. Prentice-Hall Inc., p. 706.